Check for updates

Highly Efficient n-Doping via Proton Abstraction of an Acceptor₁-Acceptor₂ Alternating Copolymer toward Thermoelectric Applications

Adrian Hochgesang, Andreas Erhardt, John Mohanraj, Meike Kuhn, Eva M. Herzig, Selina Olthof, and Mukundan Thelakkat*

Electron transporting (*n*-type) polymers are the coveted complementary counterpart to more thoroughly studied hole transporting (*p*-type) semiconducting polymers. Besides intrinsic stability issues of the doped form of *n*-type polymer toward ubiquitous oxidizing agents (H_2O and O_2), the choice of suitable *n*-dopants and underlying mechanism of doping is an open research field. Using a low LUMO, *n*-type unipolar acceptor₁-acceptor₂ copolymer poly(DPP-TPD) in conjunction with bulk *n*-doping using Cs_2CO_3 these issues can be addressed. A solid-state acid-base interaction between polymer and basic carbonate increases the backbone electron density by deprotonation of the thiophene comonomer while forming bicarbonate, as revealed by NMR and optical spectroscopy. Comparable to N-DMBI hydride/electron transfer, Cs_2CO_3 proton abstraction doping shifts the poly(DPP-TPD) work function toward the LUMO. Thereby, the anionic doped state is resilient against O_2 but is susceptible toward H_2O. Based on GIWAXS, Cs_2CO_3 is mostly incorporated into the amorphous regions of poly(DPP-TPD) with the help of hydrophilic side chains and has minor impact on the short-range order of the polymer. Cs_2CO_3 proton abstraction doping and the acceptor₁-acceptor₂ copolymer architecture creates a synergistic *n*-doped system with promising properties for thermoelectric energy conversion, as evidenced by a remarkable power factor of $(5.59 \pm 0.39) \times \mu W\ m^{-1}\ K^{-2}$.

1. Introduction

Organic semiconductors (OSCs) offer unique benefits over their inorganic counterparts, most notably the solution processability, flexibility, and chemical structure tailoring leading to tunable electronic properties. These properties allow them to be employed in a multitude of applications previously dominated by inorganic semiconductors, such as organic photovoltaics, organic field-effect transistors, or organic light-emitting diodes.[1–3] Pristine organic semiconductors are of intrinsic nature, implying a low free carrier density well within the realm of electrical insulators. Manipulation of the charge carrier density via chemical doping is a crucial tool to transform intrinsic semiconductors into conducting unipolar materials. Most notably, doping results in an increase in electrical conductivity.[4] The resulting doped materials can, for example, be applied as charge transport layers in solar cells or as active materials in thermoelectric generators.[5,6] Chemical doping processes are redox reactions (oxidation for *p*-type materials, reduction for *n*-type materials), resulting in polarons on the host material. The doped system consists of two parts, the OSC and the dopant; each of which we will focus on separately.

Donor–acceptor (abbr. D–A) polymers are a popular approach for high-performance *n*-type OSCs. By combining electron-deficient acceptor and electron-rich donor moieties in the polymer backbone, the band gap can be reduced by orbital overlap and HOMO and LUMO positions can be tuned separately.[7,8] A major breakthrough for *n*-type D–A OSCs was achieved by the introduction of poly(NDI2OD-T2) (N2200) by Guo et al.[9] Despite offering a field-effect electron mobility of

A. Hochgesang, A. Erhardt, M. Thelakkat
Applied Functional Polymers
University of Bayreuth
Universitätsstraße 30, 95447 Bayreuth, Germany
E-mail: mukundan.thelakkat@uni-bayreuth.de

The ORCID identification number(s) for the author(s) of this article can be found under https://doi.org/10.1002/adfm.202300614.

J. Mohanraj, S. Olthof
Department of Physical Chemistry
University of Cologne
Greinstraße 4–6, 50939 Köln, Germany

M. Kuhn, E. M. Herzig
Dynamics and Structure Formation – Herzig Group
University of Bayreuth
Universitätsstraße 30, 95447 Bayreuth, Germany

M. Thelakkat
Bavarian Polymer Institute
University of Bayreuth
Universitätsstraße 30, 95447 Bayreuth, Germany

**ADVANCED
SCIENCE NEWS**

www.advancedsciencenews.com

**ADVANCED
FUNCTIONAL
MATERIALS**

www.afm-journal.de

0.1 to 0.85 cm^2 V^{-1} s^{-1} for N2200, the structure of D–A polymers must be carefully optimized.[10] Functionalization of the electron rich monomer with electron withdrawing functionalities was demonstrated to weaken the donor character of the respective segment and thus leads to increased *n*-type character of the polymer.[11,12] The electron rich character of the donor monomer can further be increased by incorporating motifs, considered electron deficient themselves in the classical context, leading to acceptor$_1$-acceptor$_1$ homopolymers and polymers with heteroacceptor monomers (acceptor$_1$-acceptor$_2$).[13] Common acceptor units include benzobis(thiadiazole) (BBT), isoindigo (IID) or diketopyrrolo(pyrrole) (DPP) and naphthalene diimide (NDI).[14–17] Linking two different acceptor moieties (acceptor$_1$-acceptor$_2$) has distinct advantages over acceptor$_1$-acceptor$_1$ homopolymers, which suffer from high dihedral angles, loss of conjugation/planarity and as a consequence low *n*-type charge transport mobility, even though theoretical studies predicted planar structures with low dihedral angles.[18–21] For example, improved packing and coplanar backbone conformation of acceptor$_1$-acceptor$_2$ polymers was reported using fluorinated benzothiadiazole monomers in combination with NDI units by Wang et al.[22] Generally, a higher acceptor fraction of comonomers in semiconducting copolymers results in a more unipolar electron transport and lowers the LUMO value.[23] Especially the LUMO position plays two important roles in *n*-type OSCs: First, a low LUMO value ensures efficient electron injection from high work function electrodes like gold. Second, it was reported that electron acceptor materials and their respective doped states can be stable under ambient conditions if the LUMO of the pristine material exceeds 4.0 eV – a sought-after characteristic, reflected in the sparse chemical space of stable *n*-type OSCs.[24]

With these requirements in mind, we synthesized a hydrophilic alternating acceptor$_1$-acceptor$_2$ *n*-type polymer poly(DPP-TPD) (**Figure 1**).[25,26] We use the synergistic effects of a diketopyrrolopyrrole and thienopyrrolodione (TPD) acceptor to tune both HOMO and LUMO concurrently, and also to increase the stability of the *n*-doped state. Additionally, planarizing the backbone via imide C=O···H-(thiophene) non-covalent interactions and the deep HOMO energy of TPD enhance the unipolar electron transport. We tackle the problem of solubility by N-functionalization of the acceptor moieties with methoxy-capped ethylene glycol groups in both acceptor moieties. Simultaneously, these polar side chains can increase the compatibility of the polymer host material and the *n*-dopant and its counterion, as reported by Krauss et al. and Kroon et al.[27,28]

In order to *n*-dope poly(DPP-TPD), the highest (singly) occupied molecular orbital of the *n*-dopant must be located in the vicinity or lower in energy compared to the LUMO of the polymer.[29] This opens up a variety of potential *n*-dopants, one of the most popular being 4-(2,3-Dihydro-1,3-dimethyl-1H-benzimidazol-2-yl)-N,N-dimethylbenzenamine (N-DMBI) and derivatives thereof.[30–33] The *N*-DMBI *n*-doping mechanism, being based on either hydride or direct electron transfer to the OSC, has been described in detail by Bardagot et al. and Zeng et al.[32,34] Another less-thoroughly investigated *n*-type dopant is Cs$_2$CO$_3$, which is reported to effectively facilitate electron injection from a wide range of metal electrodes, when commonly applied via evaporation on top of the acceptor material, or as
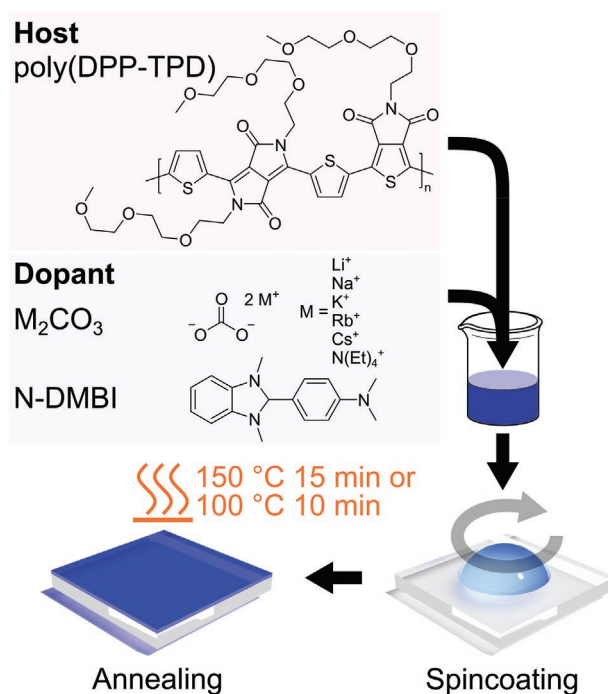

Figure 1. Device preparation and chemical structure of the *n*-type host polymer poly(DPP-TPD) as well as the investigated dopants N-DMBI and various carbonate salts.

thin individual interface layers on diverse metals in organic light emitting diodes and solar cells.[35–41] Compared to *N*-DMBI and other organic electron donors, alkali metal carbonates are a promising alternative, being far more abundant and cheaper. No detailed studies of bulk doping using carbonates have been reported so far. Moreover, only speculative explanations of the doping mechanism, ranging from integer charge transfer from either the alkali metal cation or CO$_3$$^{2-}$ to the OSC or indirect doping via the thermal degradation intermediate cesium oxide, exist.[35–41] In the context of OLED research, the viability of further alkali carbonates as *n*-type dopants has been demonstrated, suggesting redox activity of the carbonate anion.[37,42–45] Liu et al investigated the thermoelectric performance enhancement of a fullerene derivative doped by thermally evaporated Cs$_2$CO$_3$, but did not comment further on the underlying mechanism.[46] The authors like to point out the distinct difference between carbonate-doping of small molecule semiconductors such as 1,10-phenanthroline or bathocuproine and semiconducting polymers. The former has strong tendencies to complex and bind metal ions, facilitating reaction pathways not achievable in polymers.[47]

In this work, we investigate the mechanism of doping the acceptor$_1$-acceptor$_2$ polymer poly(DPP-TPD) using carbonates and evaluate the strategy toward thermoelectric applications. First, the poly(DPP-TPD) characteristics and impact of carbonate doping compared to N-DMBI on the electrical conductivity is studied. To investigate underlying electronic processes, UV/Vis/NIR spectroscopy, X-ray-, UV- and inverse photoelectron spectroscopy (abbr. XPS, UPS, IPES) as well as impedance spectroscopy, NMR and thermoelectric measurements are applied. Furthermore, the mechanism of doping is
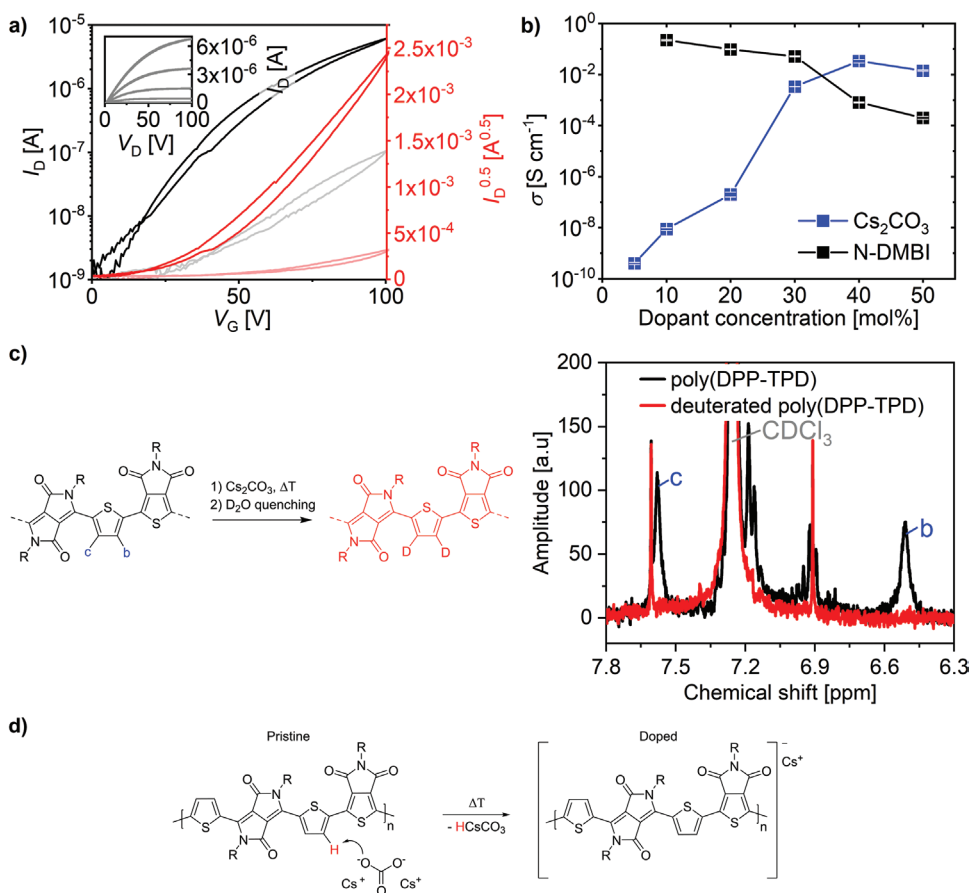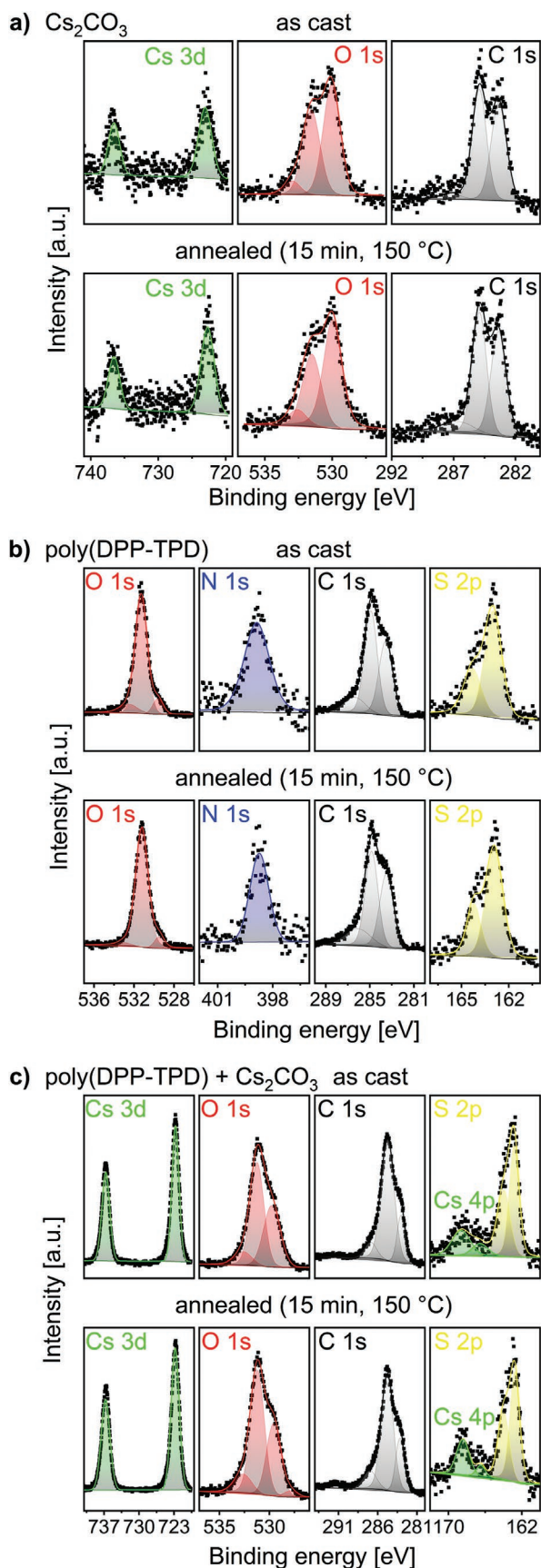
Figure 2. a) Organic field-effect transistor transfer characteristics of pristine poly(DPP-TPD). Left y-axis: Drain current I_D versus gate potential V_G, right y-axis: square root of the drain current $I_D^{0.5}$ versus gate potential used for mobility determination (see Supporting Information). The inset shows the output characteristics with gate voltage variation from 0 to 100 V in 20 V steps. b) Thin film conductivity values of poly(DPP-TPD), doped with various amounts of N-DMBI and Cs_2CO_3. c) Left: Sketch showing the deprotonation and subsequent deuteration mechanism of the poly(DPP-TPD) backbone. Right: ^{1}H-NMR of pristine poly(DPP-TPD) in $CDCl_3$ (black curve) showing the two signals b and c of the thiophene protons of the poly(DPP-TPD) backbone. After doping with Cs_2CO_3 and quenching the doped poly(DPP-TPD) in D_2O, the corresponding positions are deuterated and not visible in the NMR spectrum (red curve). d) Proposed Brønsted acid-base doping mechanism between Cs_2CO_3 and poly(DPP-TPD).

elucidated. Finally, grazing-incidence wide-angle X-ray scattering (GIWAXS) and scanning electron microscope (abbr. SEM) measurements are employed to determine the morphology and topology of poly(DPP-TPD) and changes thereof during doping.

2. Discussion

All the synthetic details of the monomers and polymer and their characterization are given in the supporting information. In short, direct arylation polymerization was used to obtain the polymer with an average molecular weight of 20.6 kg mol^{-1} (GPC).[48] To understand the charge transport properties of this strong acceptor$_1$-acceptor$_2$ copolymer poly(DPP-TPD), we fabricated field-effect transistors and measured the output- and transfer characteristics (**Figure 2**a, full transfer scan in shown in Figure S1, Supporting Information). We recorded an average electron mobility of $\mu_e = 4.4 \times 10^{-4}$ cm^2 V^{-1} s^{-1} with very little current flowing in the *p*-type region, rendering poly(DPP-TPD) suitable as a host for *n*-doping experiments.

In a first step, the feasibility of bulk doping of poly(DPP-TPD) using Cs_2CO_3 was examined via electrical conductivity measurements of the doped systems. Cesium carbonate and N-DMBI (as a reference) were mixed with poly(DPP-TPD) in different doping concentrations. The solutions were spin coated onto interdigitated Au electrodes from HFIP solutions under glovebox conditions (<1 ppm H_2O and O_2). The thin film conductivities σ were obtained from the slope of linear I/V-curves and geometric parameters (See Supporting Information for details). It was found, that both dopants require thermal activation for the doping reaction to proceed (Figure 6a). Hence, the substrates were annealed at 150 °C for 15 min (Cs_2CO_3) or 100 °C for 10 min (N-DMBI) under inert atmosphere. Figure 2b summarizes the thin film conductivities of Cs_2CO_3 and N-DMBI doped poly(DPP-TPD). Both dopants induce an increase in σ over multiple orders of magnitude compared to pristine poly(DPP-TPD) (1.0×10^{-11} S cm^{-1}). In the case of N-DMBI doping the highest conductivity value of 0.22 S cm^{-1} was achieved at 10 mol.% dopant concentration; the conductivity slowly decreasing up to 30 mol.% and radically above this level of doping. We argue that the loss in σ upon exceeding

**ADVANCED
SCIENCE NEWS**

www.advancedsciencenews.com

**ADVANCED
FUNCTIONAL
MATERIALS**

www.afm-journal.de

Figure 3. XPS detail spectra of a) Cs_2CO_3, b) pristine poly(DPP-DTT) and c) poly(DPP-TPD) doped with 30 mol.% Cs_2CO_3 O 1s, N 1s, C 1s and S 2p regions. The spectra were recorded before (upper panels) and after (lower panels) annealing. Black squares are data points, lines are the fitted spectra and shaded areas the deconvoluted contributions to the total fitted spectrum.

10 mol.% N-DMBI originates from doping efficiency losses. As shown later, in the case of N-DMBI and Cs_2CO_3, the dopant is accumulated in fully amorphous polymer regions.

We observe a stark contrast between N-DMBI reaching the highest conductivity at 10 mol.% (0.22 S cm^{-1}) and carbonates showing a saturation effect starting from 30 mol.% and a maximum conductivity of 0.034 S cm^{-1}. The discrepancy and trend in σ hints toward different doping reactions for both dopants. To verify the feasibility of bulk doping by Cs_2CO_3, we measured the absolute values of ionization potential and electron affinity using inverse and regular UPS experiments on Cs_2CO_3 and poly(DPP-TPD) thin films (Tables S1–S5 and Figure S2, Supporting Information). An ionization potential of (6.5 ± 0.11) eV for Cs_2CO_3 was determined, far exceeding the electron affinity of poly(DPP-TPD) (3.3 ± 0.60) eV. Thus, an electron transfer from Cs_2CO_3 HOMO to poly(DPP-TPD) LUMO is energetically unfavorable.

By impedance spectroscopy, we studied the contribution of ion diffusion (by Cs^+ or CO_3^{2-}) to the observed current flow. For this, Poly(DPP-TPD) was dissolved in HFIP, doped with 30 mol.% Cs_2CO_3 and spun-cast onto interdigitated Au electrodes. After annealing at 150 °C for 15 min, the electrical impedance was recorded under inert atmosphere before and after polarization at 5 V for 40 min. The phase angle ϕ of the current flowing through the device remains constant at $0°$ between 10 Hz and 10 mHz independent of polarization, indicating purely ohmic behavior without diffusion processes (Figure S3, Supporting Information).

To verify if the annealing leads to the formation of side products such as Cs_2O and if it contributes to doping, we conducted XPS spectroscopy as follows. The C 1s, O 1s and Cs 3d core level peaks of Cs_2CO_3 powder were monitored at rt and after in situ heating to 150 °C for 15 min under vacuum (**Figure 3**). No change in peak area or position occurred, hence the absence of Cs_2CO_3 side-products during the doping experiments can be concluded. TGA measurements on Cs_2CO_3 powder affirm this with a decomposition onset temperature of > 500 °C (Figure S4, Supporting Information). In contrast to Cs_2CO_3, which is stable at these conditions, Li_2CO_3 shows minor degradation in XPS studies (Figure S5, Supporting Information). Besides the carbonate C 1s peak at 291 eV, a lower BE component at 285 eV increased in intensity after annealing.[49] We attribute the lower BE C 1s peak to either bicarbonate formation or C−C bonds formed during decomposition.[50] Having excluded ion diffusion and dopant decomposition, we turn our attention toward alternative reaction pathways to explain the mechanism of n-doping poly(DPP-TPD) with carbonates.

To gain deeper insight on the mechanism of the n-doping process using carbonates, XPS analysis on thin poly(DPP-TPD) and Cs_2CO_3 films coated onto quartz substrates as well as doped films was conducted (Figure 3). The C 1s peaks of pristine poly(DPP-TPD) appear at 283.5, 285 and 286 eV, originating

from sp^2 C=C, sp^3 C—C and C—O—C ethylene glycol side chain binding energies (convoluted with C=O), respectively.[51,52] O 1s of poly(DPP-TPD) has distinct binding energies at 529.5 eV (aromatic C=O), 531.3 eV (C—O—C side chain) and 532.8 eV (Si-O-Si substrate).[53,54] Sulfur of the poly(DPP-TPD) thiophene donor moiety was detected at 162.9 eV (2p$_{3/2}$) and 164.2 eV (2p$_{1/2}$), consistent with measurements on DPP-DTT by Wei et al.[55] N 1s could not be resolved in pristine poly(DPP-TPD) XPS experiments. The pristine poly(DPP-TPD) film sample was annealed at 150 °C for 15 min under vacuum and the photoelectron spectrum was recorded again. We observed no change in peak position or intensity, therefore we conclude the polymer to be stable under annealing conditions used for Cs$_2$CO$_3$ doping.

Next, a doped system consisting of 30 mol.% Cs$_2$CO$_3$ in as cast and annealed state was analyzed using XPS (Figure 3). We selected a higher pass energy of 55 eV and many integration cycles of 12 to resolve components with a low atomic concentration such as N 1s. The samples were heated at 150 °C for 15 min under an inert atmosphere to promote the doping reaction and subsequently, the XPS spectra were recorded after cooling back to rt. No significant change in O 1s and N 1s peak positions and intensities were recorded before and after annealing. In doped samples, an additional C 1s peak at 291.3 eV emerges, associated with the π-π* shake-up peak or aromatic systems.[56,57] Further, two high BE peaks at 166.8 and 168.8 eV appear in the S 2p region, which are absent in the pure poly(DPP-TPD) spectrum. To identify the origin of these peaks, we also replaced Cs$_2$CO$_3$ with the alkali-metal free bis(tetraethylammonium)carbonate (NEt$_4$)$_2$CO$_3$ as dopant and repeated the XPS experiment on doped poly(DPP-TPD). In this case, no high BE peaks were recorded between 165 and 170 eV before and after annealing at 150 °C for 15 min (Figure S6, Supporting Information). This led us to believe that the peaks at 166.8 and 168.8 eV are originating from Cs 4p transitions at the sample surface and are not associated with highly oxidized sulfur species. Similarly, the Cs 3d peaks located at 736.8 eV (Cs 3d$_{3/2}$) and Cs 3d$_{5/2}$ at 722.7 eV did not change position, intensity or full width at half maximum (FWHM) during annealing (Figure 3). Chen et al. and Wu et al. reported a shift of the Cs 3d binding energy toward higher energies in experiments involving evaporated Cs$_2$CO$_3$ as interlayers between electron transport layer and metals and related it to electron transfer from Cs to semiconductor.[35,58] Nevertheless, no such shift was found in our experiment. This finding confirms the neutral role of the Cs$^+$ spectator cation in bulk doping of poly(DPP-TPD). We also infer from XPS results, that the polymer backbone is not subject to chemical degradation during doping.

As the only remaining species, the interaction between CO$_3$$^{2-}$ and poly(DPP-TPD) was investigated in detail with ATR-FTIR spectroscopy under anhydrous conditions (Figure S7, Supporting Information). A 30 mol.% Cs$_2$CO$_3$ doped poly(DPP-TPD) powder was prepared by removing the solvent under vacuum after stirring the doped HFIP solution for 5 min at rt. ATR-FTIR spectra were measured before and after annealing under inert atmosphere at 150 °C for 15 min. The resulting spectra are compared to the pristine poly(DPP-TPD) polymer. Upon thermal treatment, a distinct sharp transition appears at 2918 cm^{-1}, assigned to O-H stretching vibrations. As water was excluded during measurement, we argue this peak to originate

from HCO$_3$$^-$ formed during doping. This was confirmed by ATR-FTIR of CsHCO$_3$ powder (Figure S7, Supporting Information).[59] As the experiment was conducted in the solid state, we conclude that the poly(DPP-TPD) has to be deprotonated during the annealing process to form HCO$_3$$^-$ species. Further, a shift in the C—O—C ether stretching modes from 1093 cm^{-1} (in pristine poly(DPP-TPD)) to 1086 cm^{-1} after doping and annealing was observed, which can be attributed to coordination of Cs$^+$ cations by the ethylene glycol side chains.[60,61] As the ethylene glycol side chain protons are not in conjugation with the main chain, deprotation leading to enhanced conductivity has to occur at the polymer backbone. The sole protons of poly(DPP-TPD) are located at the 3,4 thiophene positions. Deprotonation leads to a strong increase in unsaturated C-H vibration at 1016 cm^{-1}.[62,63] as observed in FTIR (Figure S7, Supporting Information)

Based on our findings, we propose a Brønsted acid-base interaction between Cs$_2$CO$_3$ and poly(DPP-TPD) during doping, deprotonating the thiophene moiety and forming CsHCO$_3$ as a product. To verify the proton abstraction mechanism, ^{1}H-NMR spectroscopy was conducted. The thiophene protons of the pristine poly(DPP-TPD) polymer are detected downfield at 6.51 and 7.58 ppm. The authors note that even prolonged stirring in CDCl$_3$ at rt causes no change in the thiophene proton peak integral, hence the pristine polymer does not exchange protons with the solvent without dopant. If our hypothesis holds true, quenching the Cs$_2$CO$_3$ doped poly(DPP-TPD) in D$_2$O should cause the thiophene anion to be deuterated, rendering them invisible to the proton NMR. To prove this experimentally, we prepared a poly(DPP-TPD) HFIP solution, to which a 1:1 molar ratio of Cs$_2$CO$_3$ in aqueous solution was added. After removing the solvent under vacuum at 50 °C, the solid mixture was transferred to a glovebox, annealed at 150 °C for 15 min in the solid state and immediately quenched with D$_2$O. Afterward, a ^{1}H-NMR spectrum was recorded again in CDCl$_3$ (Figure 2c). Both proton signals are missing in the quenched spectrum, hence we conclude the proposed deprotonation (or proton abstraction) mechanism to be correct (Figure 2d). The peak at ≈ 7.1 ppm can be assigned to thiophene protons of homocoupling defects, i.e., two thiophene monomers are directly coupled during the direct arylation polymerization reaction. As these protons are also labile, they too are absent in the ^{1}H-NMR spectrum after deprotonation and deuteration. Further, we note, that the side chain protons are not affected by the doping procedure (See Figures S8 and S9, Supporting Information for full ^{1}H-NMR spectra).

Based on the proposed proton abstraction mechanism, we argue that less basic carbonates should induce a lower density of negative charges on poly(DPP-TPD) or do so with a higher activation energy. We investigated the impact of carbonate basicity by monitoring the thin film conductivity of poly(DPP-TPD) doped with different carbonates such as Li$_2$CO$_3$, Na$_2$CO$_3$, K$_2$CO$_3$ and Rb$_2$CO$_3$. Poly(DPP-TPD) was dissolved in HFIP with varying amounts of aqueous dopant stock solution added and spin coated onto interdigitated Au electrodes. Within the series of alkali metal carbonates, the maximum achieved conductivity correlates with the increasing cation ionic radius and in turn the carbonate basicity (**Figure 4**a).[64] Particularly the soft Lewis acids Cs$^+$ and Rb$^+$ ion help to improve the doping efficiency by increasing the alkali metal carbonate basicity.[65] Though
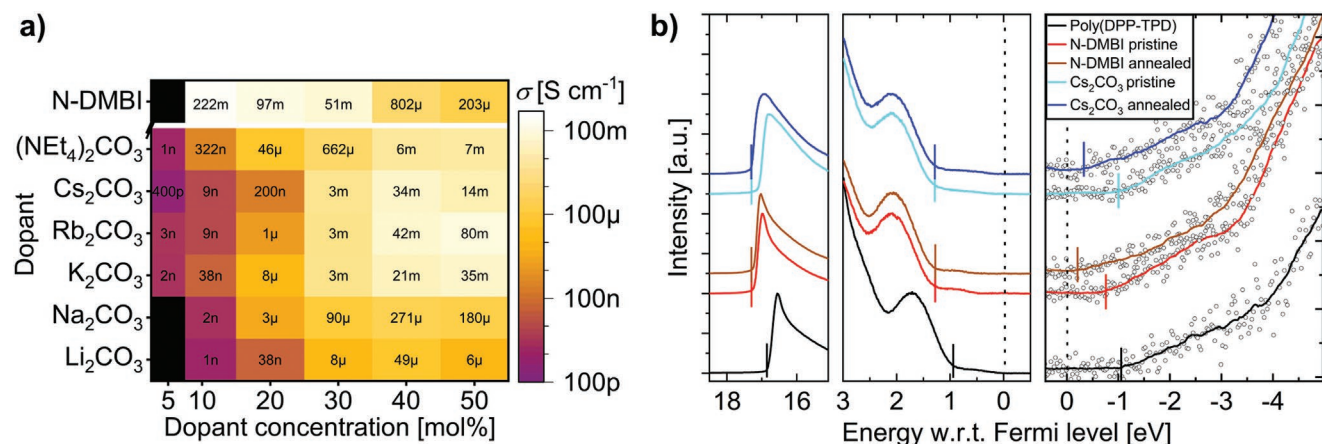
Figure 4. a) Heat map of dopant- and doping content dependent conductivity of poly(DPP-TPD) with various alkali metal carbonates, as well as $(NEt_4)_2CO_3$ and N-DMBI. Conductivity was extracted in all cases from the linear slope of the I–V characteristics of the solution processed materials between interdigitated gold electrodes on Si/SiO₂ substrates. b) Frontier orbitals of poly(DPP-TPD) (black lines) doped with N-DMBI (pristine: red lines, annealed at 100 °C for 10 min under inert conditions: dark brown lines) and Cs_2CO_3 (pristine: cyan lines, annealed at 150 °C for 15 min under inert conditions: dark blue lines). Secondary electron cutoff (left) and valence band maximum (middle) were measured by UPS, conduction band minimum (right) by IPES.

HFIP exerts a considerable Brønsted acidity, we found no correlation to the doping reaction, as it also proceeds in strictly anhydrous aprotic solvents and occurs only in solid state during annealing. Specifically, poly(DPP-TPD), doped with 30 mol.% Cs_2CO_3 exhibits a conductivity of $(1.9 \pm 0.31) \times 10^{-4}$ S cm⁻¹, when cast from a mixture of hot DMSO and NMP (Figure S10, Supporting Information). However, the host polymer is only sparsely soluble in the used solvent mixture, resulting in heterogeneous films and thus decreased conductivity. Further, in contrast to earlier literature affiliating Cs⁺ with the n-doping reaction, we could replace the alkali metal ions with an all organic bis(tetraethylammonium) cation in the doping experiment, forming $(NEt_4)_2CO_3$.[35] After annealing poly(DPP-TPD) thin films mixed with $(NEt_4)_2CO_3$, the dopant reacts similar to the inorganic carbonates tested, showcasing the neutral role of the cations in this study (Figure 4a). We argue that the carbonate lattice energy plays a decisive role in deprotonating the thiophene donor moiety, ultimately leading to enhanced electrical conductivity. Summarizing, electrical conductivity, XPS, NMR and ATR-FTIR measurements fortified the role of the carbonate anion as the active species during a proton abstraction doping mechanism. Via counter ion choice, the carbonate basicity and hence dopant activity can even be tailored. Moreover, this is not specific for Cs_2CO_3, but common to any carbonate, even an organic carbonate such as bis(tetraethylammonium) carbonate.

2.1. Frontier Orbital Measurement

Charge carrier density changes on the host due to doping are usually directly reflected in a change of the work function, i.e., the Fermi position E_F. It is generally accepted, that n-doping leads to an E_F upward shift toward the LUMO position, increasing the hole injection barrier (abbr. HIB, the distance between E_F and HOMO) and concurrently decreasing the electron injection barrier (distance between E_F and LUMO).[30,66] To quantify the E_F shift, we measure UPS and IPES on 30 mol.%

N-DMBI and Cs_2CO_3 doped poly(DPP-TPD) thin films, which were prepared on top of ITO/PEDOT:PSS substrates. The doped films were measured before and after annealing under inert atmosphere. As our carbonate case study involves a deprotonation step that is fundamentally different from simple electron transfer, we refrain from frontier orbital models based on integer charge transfer or charge transfer complex formation.[67,68] First, we address the 30 mol.% N-DMBI doped poly(DPP-TPD) reference system. Relative to pristine poly(DPP-TPD), the HIB increases from (1.0 ± 0.10) eV to (1.3 ± 0.10) eV in the doped system (Figure 4b and Table S1, Supporting Information). Concurrently, the electron injection barrier is decreased from (1.1 ± 0.60) eV to (0.20 ± 0.60) eV. Therefore, poly(DPP-TPD) is n-doped by N-DMBI; the doping mechanism being either hydride or electron transfer from N-DMBI as reported earlier by Bardagot et al. and Zeng et al.[32,34] Next, the dopant was changed to Cs_2CO_3 (30 mol.%) and the UPS spectrum recorded again. Similar to N-DMBI, the HIB changes from (1.0 ± 0.10) eV in pristine poly(DPP-TPD) to (1.3 ± 0.10) eV after annealing with Cs_2CO_3, while the electron injection barrier decreases from (1.1 ± 0.60) eV to (0.30 ± 0.60) eV (Figure 4b and Table S2, Supporting Information). We conclude that the proton abstraction by CO_3^{2-} leads to a shift of the Fermi level toward the LUMO of poly(DPP-TPD), thus n-doping the polymer.

We also note that the LUMO of both N-DMBI and Cs_2CO_3 doped poly(DPP-TPD) shifts to lower values, whereas the HOMO position remains constant. However, the electron affinity is not expected to change during chemical doping, which is also confirmed by UV/Vis/NIR measurements on poly(DPP-TPD) thin films doped with 30 mol.% Cs_2CO_3 (Figure S11, Supporting Information). No significant changes occurred after annealing, demonstrating a stable band gap. This suggests that the onset of the unoccupied states observed for the Cs_2CO_3 doped samples is not LUMO, but rather originates from gap states that form in this film. The origin of these states positioned at ca. $0.30 - 0.50$ eV below the pristine poly(DPP-TPD) LUMO at (3.3 ± 0.6) eV, however, remains obscure.

**ADVANCED
SCIENCE NEWS**

www.advancedsciencenews.com

**ADVANCED
FUNCTIONAL
MATERIALS**

www.afm-journal.de

Having quantified the position of the frontier orbitals in doped and pristine poly(DPP-TPD), we can correlate the stability of the doped state to the proposed proton abstraction mechanism. The LUMO position plays a decisive role in stability considerations of conventional n-doped organic semiconductors (by means of either hydride or electron transfer): If the LUMO of the pristine polymer is situated below 3.7 eV, the n-doped state is stable with respect to the reduction of H_2O, whereas if it is even lower (<4.0 eV), it is resilient against both H_2O and O_2 reduction (achieving "ambient stability").[24,69] Based on these findings, we expect Cs_2CO_3 doped poly(DPP-TPD) to be unstable against oxidation by H_2O and O_2 with $E_{LUMO} = (3.6 \pm 0.6)$ eV (Table S2, Supporting Information). To study the ambient stability of Cs_2CO_3 doped polymer, we drop-casted poly(DPP-TPD) doped with 30 mol.% Cs_2CO_3 onto interdigitated electrodes under inert atmosphere. The doped substrates were transferred into a Schlenk flask, and the electrodes connected to a potentiostat to record the current overtime at fixed potential of 1 V, monitoring the change in conductivity. At one point, the samples are exposed to either ambient atmosphere (38 % relative humidity, 26 °C), 95 % relative humidity atmosphere (28 °C) or pure dry oxygen (Figure S12, Supporting Information). It is to be noted that in both ambient atmosphere as well as high humidity atmosphere, dissolved oxygen in moist air is present compared to just dry oxygen that has no moisture in it. The doped state is far more resilient toward dry O_2 than H_2O+O_2 in the atmosphere. We conclude that the stability of poly(DPP-TPD) doped by proton abstraction is mostly governed by the presence of H_2O.

2.2. Impact of Doping on the Polymer Microstructure

Complimentary to previous mechanistic considerations, the impact of doping on the polymer topology and morphology was investigated. To evaluate possible de-mixing of the doped materials at high doping contents, SEM images of the pristine polymer were compared to poly(DPP-TPD) doped with 30 mol.% N-DMBI or Cs_2CO_3 (**Figure 5**, for comparison with non-annealed samples see Figures S13 and S14, Supporting Information). Upon high magnification, a structure or patterns are recognizable for all samples. It was concluded to be caused by the fast-evaporating solvent used for film fabrication rather than dopant segregation, as the inhomogeneous features are as pronounced in the undoped polymer as in the doped systems. To study the dopant aggregation of poly(DPP-TDP) in detail, atomic force microscopy (AFM) was conducted in tapping mode on doped and pristine thin films (Figure 5; Figure S15, Supporting Information). A similar structure as in SEM-experiments caused by the fast evaporation of HFIP during film preparation is observed in all films. No change in topography was detected for pristine poly(DPP-TPD) before and after annealing at 150 °C for 15 min. After doping with 30 mol.% N-DMBI, no aggregates were found on the surface of the film before and after annealing. This is in agreement with AFM experiments by Ye et al. who reported excellent solubility of N-DMBI in n-type semiconducting polymers with glycol ether side chains.[70] For Cs_2CO_3 doped poly(DPP-TPD), phase-separated particles are detected, which increase in size and surface density after annealing. Based on our proposed doping

mechanism (Figure 2d), we argue that the observed particles are composed of $CsHCO_3$ after annealing. In this context, we like to mention that the alkylated Poly(DPP-TPD) counterpart with branched C_8H_{17}-C_6H_{13} side chains is very poorly miscible with Cs_2CO_3 and neither uniform films nor reproducible data could be obtained from those doped films.

Deeper insight into the thin film morphology was attempted using GIWAXS experiments, performed on the pristine as well as doped polymer on Si/SiOx substrates. Intensive 100 signals at $Q_{xy} = 0.31$ Å^{-1}, corresponding to the polymer-polymer lamellar distance and 010 reflexes at $Q_z = 1.75$ Å^{-1}, caused by the polymer π-π stacking are revealed (Figure 5d). The absence of higher order peaks, however, indicates a low overall ordering in all investigated materials. Upon thermal annealing of the as-cast materials, the peak FWHM determined from line-cuts does not change, suggesting no significant change of domain size (Figure S16, Supporting Information). The low structural impact of annealing can be explained by the high melting point of the host polymer, which could not be detected using DSC experiments up to 200 °C (Figure S17, Supporting Information). Using Flash-DSC, we could extend the temperature range past the decomposition temperature of poly(DPP-TPD) by recording the heat flow at large heating and cooling rates up to 2000 K min^{-1} (Figure S18, Supporting Information). The absence of phase transitions in both experiments shows the overall amorphous behavior of the sample.[71]

Thus, annealing for 15 min at $T = 150$ °C does not enable sufficient polymer segment mobility to enable the formation of highly ordered structures. Despite the poor ordering, a preferential face-on orientation of the polymers with respect to the substrate can be seen in most cases. Interestingly, the N-DMBI doped samples did form this oriented structure only during thermal treatment, while samples without any dopant and with added Cs_2CO_3 demonstrated a preferential orientation already before thermal treatment. Line cuts of the undoped polymer reveal that the π-π stacking signal is the sum of two overlapping signals. By comparison of the vertical (ver) and horizontal (hor) cut, a significant shift of the peak ratios can be seen, suggesting that the sharp signal at q = 1.75 Å^{-1} corresponds predominantly to a short range ordered, oriented material fraction, while the second signal at q = 1.46 Å^{-1} is caused by isotropically distributed short range ordered material, where a slightly larger π-π stacking distance is realized.

Molecular rearrangements during the doping process of poly(DPP-TPD) with N-DMBI can be monitored by comparison of the scattering patterns of undoped and doped materials. Compared to neat poly(DPP-TPD), the N-DMBI doped films show slightly broader 100 signals, suggesting a reduced short-range order caused by dopant incorporation. However, the absence of a shift in the peak position shows that dopant molecules do not affect lamellar expansion of the host material and thus likely do not accumulate there. Instead, location in the fully amorphous domains can be assumed. 010 signals of annealed poly(DPP-TPD) and annealed N-DMBI doped material are identical, indicating no structural change in the π-π stacking. The deviation of the material prior to annealing (see line cuts in Figure S16, Supporting Information) can be explained by the reorientation of isotropic domains to face-on ordered domains.
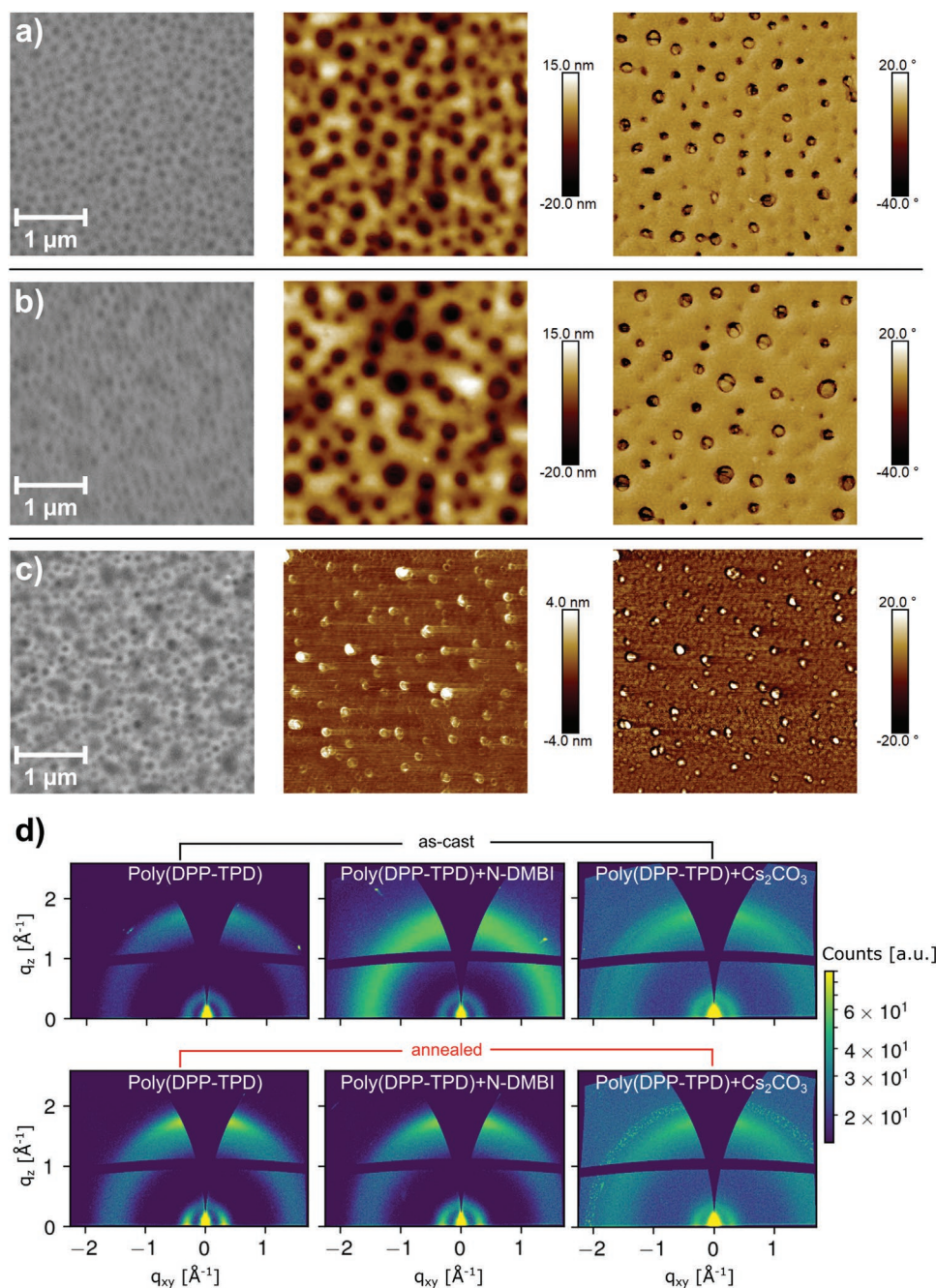
Figure 5. SEM micrographs (50k magnification, left) and AFM tapping mode images (middle: topography, right: phase) of a) pristine poly(DPP-TPD) b) poly(DPP-TPD) doped with 30 mol.% N-DMBI and c) poly(DPP-TPD) doped with 30 mol.% Cs_2CO_3. All films were annealed (N-DMBI doped samples: 100 °C, 10 min, Cs_2CO_3 doped and pristine samples: 150 °C, 15 min) prior to measurement. d) 2D-GIWAXS patterns of pristine poly(DPP-TPD) (left), poly(DPP-TPD) doped with N-DMBI (middle) and poly(DPP-TPD) doped with Cs_2CO_3 (right). The upper panels show the as-cast samples, the lower panels after annealing under inert atmosphere (N-DMBI: 100 °C, 10 min, Cs_2CO_3: 150 °C, 15 min).

In a similar matter, the structural changes correlated to Cs_2CO_3 doping can be investigated. Compared to pristine poly(DPP-TPD), only insignificant changes in FWHM and q-value of the 100 signals are apparent in the vertical line cut (Figure S16, Supporting Information), hinting no substantial change of coherence length and lamellar distance. Likewise, upon annealing, only small shifts of the scattering signal peaks are observable, if at all. The most pronounced changes

of approximately −0.02 Å^{-1} are found in the 100 signals of the polymer doped with Cs_2CO_3. These signal shifts, however, lie in the margin of error for the measurement, e.g., caused by deviations in sample position between measurements. Therefore, we consider this change as insignificant and conclude that the majority of dopant must be located in the amorphous domains. 2D scattering images as well as line cuts reveal the presence of ordered impurities in the Cs_2CO_3 doped samples at q values of
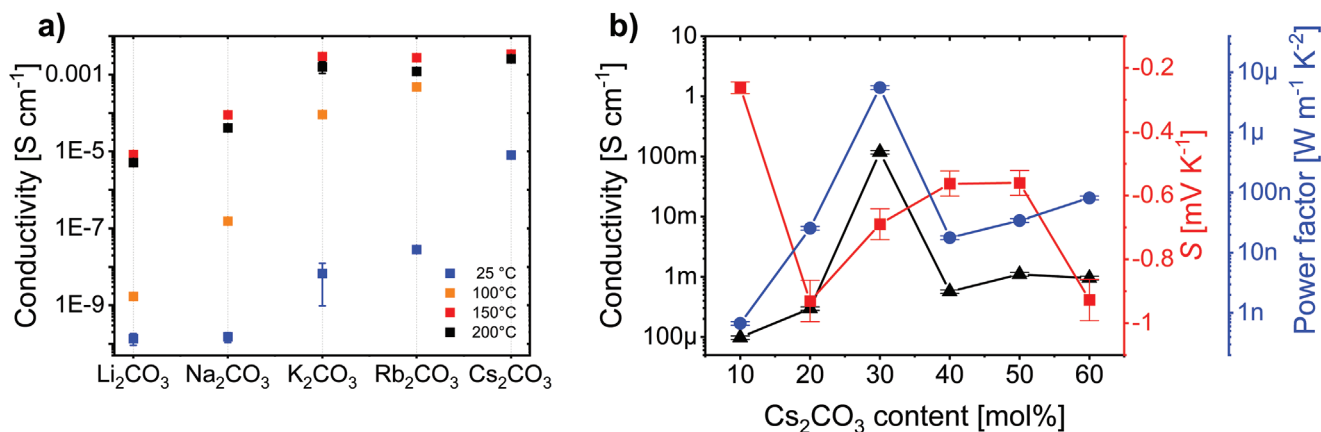
**ADVANCED
SCIENCE NEWS**

www.advancedsciencenews.com

**ADVANCED
FUNCTIONAL
MATERIALS**

www.afm-journal.de

Figure 6. a) Temperature dependent conductivity of poly(DPP-TPD) doped with 30 mol.% of Li_2CO_3, Na_2CO_3, K_2CO_3, Rb_2CO_3 and Cs_2CO_3 after annealing at different temperature for 15 min each consecutively. The data points for Cs_2CO_3 annealed at 100, 150 and 200 °C are closely grouped. b) Thermoelectric properties of poly(DPP-TPD) as a function of the Cs_2CO_3 doping ratio. Black triangles: Thin film conductivity, red squares: Seebeck coefficient, blue circles: power factor.

$Q = 1.41$ Å^{-1} and $Q = 1.95$ Å^{-1} in the pristine and $Q = 2.07$ Å^{-1} in the annealed state. These impurities are initially mostly short-range ordered with defined peaks suggesting a small amount of long-range order (Figure S16, Supporting Information). Interestingly, the original peaks obtained from the ordered domains change position during annealing. This agrees well with the proposed doping reaction, where Cs_2CO_3 is consumed during annealing to form $CsHCO_3$, leading to different scattering patterns of the inhomogeneities. We argue that the $CsHCO_3$ forms individual crystallites with random orientation after annealing, resulting in well-defined Bragg peaks.

2.3. Thermoelectric Performance

The competitive electrical conductivity of proton abstraction doping compared to N-DMBI doping enables possible use of such doped polymers in thermoelectric energy conversion. First the temperature dependence of doping using various alkali metal carbonates at different annealing temperatures of 25, 100, 150 and 200 °C was studied by measuring the electronic conductivity of the resulting doped polymers using 30 mol.% dopants (**Figure 6**a). It is obvious that the conductivity for lower annealing temperatures scales with the basicity and ion radius of the alkali metal carbonate as explained in Figure 4a. However, at 150 °C and above, all the three carbonates, K_2CO_3, Rb_2CO_3 and Cs_2CO_3 show saturation conductivities. To quantify the thermoelectric properties of the pristine and Cs_2CO_3-doped poly(DPP-TPD), the polymer was dissolved in HFIP with varying amounts of dopant and drop-casted onto Al_2O_3 substrates. The sample was mounted on to a thin film adapter of the ZEM-3 thermoelectric system and annealed in situ under 0.8 bar helium atmosphere at 150 °C for 15 min prior to measurement. Throughout the range of 10 – 60 mol.% Cs_2CO_3, the Seebeck coefficient S exerts a negative sign, a fingerprint for electron majority carriers (Figure 6b).

We conclude that the intragap states observed in UPS experiments are most likely localized and charge transport is dominated by the LUMO states lower in energy. Since

conductivity is the highest at 30 mol.% doping, the power factor $PF = \sigma S^2$ of 30 mol.% Cs_2CO_3 doped poly(DPP-TPD) shows a maximum with $PF = (5.6 \pm 0.39) \times 10^{-6}$ W m^{-1} K^{-2} (For full data see Table S6, Supporting Information). Between 20 mol.% and 50 mol.%, S decreases by a factor of ≈ 0.5 from (931 ± 65.1) µV K^{-1} to (560 ± 39.2) µV K^{-1}. We attribute this loss in Seebeck coefficient to the decreased distance between Fermi level and mean energy of charge carriers (here approximated with the conduction band minimum, e.g. LUMO, see Figure 4b) upon doping, a phenomenon well documented in literature.[72,73] The PF maximum is mostly governed by the conductivity maximum at 30 mol.%, which is not only observed for Cs_2CO_3, but also for Na_2CO_3 and Li_2CO_3 (Figure 4a, Rb_2CO_3 and $(NEt_4)_2CO_3$ level off significantly). Combined with the observed crystallite formation in GIWAXS and AFM experiments, we argue that the crystallization of both carbonate and bicarbonate causes less dopants to be available for the deprotonation reaction as opposed to a homogeneously mixed polymer:dopant system at lower doping ratios.

This thermoelectric performance is competitive toward recently published *n*-type acceptor-acceptor polymers. Wang et a reported a naphthalenediimide-bithiazole based acceptor-acceptor copolymer poly(NDI2OD-Tz2), which achieved a PF of 1.5×10^{-6} W m^{-1} K^{-2} upon vapor-doping with tetrakis(dimethylamino)ethylene.[74] Liu et al. characterized the thermoelectric performance of the similar all-acceptor copolymer PNDI2TEG-2Tz with hydrophilic ethylene glycol side chains and achieved a PF of $(4.5 \pm 0.2) \times 10^{-6}$ W m^{-1} K^{-2}, doped with 21 mol.% N-DMBI.[75] Using a pyridine-flanked DPP-core, Yang et al. synthesized the polymer PDPF with a PF of $(4.65 \pm 0.23) \times 10^{-6}$ W m^{-1} K^{-2} with 5 mol.% N-DMBI.[76] By introducing the even more electron-deficient acceptor pyrazine as a DPP flanking unit in conjunction with 3,3′-dicyano-2,2′-bithiophene comonomers, Yan et al. demonstrated a PF of 57.3×10^{-6} W m^{-1} K^{-2} with 40 mol.% N-DMBI.[77] To the best of our knowledge, this is the first report of double donor-acceptor polymers doped with common carbonates for thermoelectric applications and opens up new possibilities toward alternative

**ADVANCED
SCIENCE NEWS**

www.advancedsciencenews.com

**ADVANCED
FUNCTIONAL
MATERIALS**

www.afm-journal.de

doping pathways to obtain very high conductivity as well as appreciably good power factor.[78]

3. Conclusion

A successful synergy between a polymer semiconductor and n-dopant to form a stable and highly conductive system could lead to advances in thermoelectric research by providing the complementary counterpart to p-doped systems. By combining the concept of a hydrophilic acceptor₁-acceptor₂ copolymer poly(DPP-TPD) with proton abstraction doping, we provide a profound background to carbonate base doping and feasibility for thermoelectric applications. CO_3^{2-} is identified as the active dopant, deprotonating labile poly(DPP-TPD) thiophene protons during annealing and shifting the Fermi level toward the polymer LUMO. The conductivity hereby scales with the basicity and ion radius of the alkali metal carbonate, achieving similar performance to N-DMBI. During proton abstraction doping, no change in the short range ordered polymer microstructure was observed, probably with Cs_2CO_3 and N-DMBI residing in the fully amorphous domains of the polymer. We successfully applied the carbonate doped poly(DPP-TPD) as an n-type thermoelectric material, achieving a competitive power factor of $(5.6 \pm 0.39) \times 10^{-6}$ W m⁻¹ K⁻². These findings could pave the way for a more efficient, universal n-doping protocol of n-type semiconducting polymers, promoting both the fields of facile and efficient doping as well as the realization of organic thermoelectric generators, which is at present lacking suitable n-doped counterparts.

4. Experimental Section

General Methods: *Thermoelectric Measurement*: For thermoelectric measurements, a ZEM-3 Seebeck coefficient and resistance measurement system equipped with a high-resistance option was used. The machine was supplied by ULVAC, Japan. Aluminium oxide substrates ($0.5 \times 4 \times 10$ mm, unpolished surface) were cleaned by 15 min ultrasonication in 4 consecutive baths of 5 vol.% Hellmanex DI water, DI water, acetone, and isopropanol. The substrates were blown dry with N_2 and treated with O_3 at 50 °C for 15 min. Poly(DPP-TDP) was dissolved in HFIP (10 mg mL⁻¹). Cs_2CO_3 was dissolved in Millipore water (resistance > 20 MΩ cm⁻¹, 10 mg mL⁻¹). The appropriate amount of the Cs_2CO_3 stock solution was added to the poly(DPP-TPD) solution for a given molar ratio of dopant. The solution was drop-casted onto the aluminium oxide substrate under ambient atmosphere (50 °C, covered by petri dish to avoid coffee ring effect, 3, 30 μL doped solution). Afterward, the substrate was mounted onto the ceramic thin film holder and contacted with nickel stripes and silver paste. The silver paste was allowed to dry for a short period of time. Afterward, the sample was transferred into the measurement chamber, which was then purged by three consecutive pump-flush cycles with helium 5.0. The sample was heated to 150 °C for 15 min under 800 mbar helium atmosphere for better heat transfer. Then, the sample was allowed to cool to rt, and the measurement was started. To determine the Seebeck, two sets of base temperatures were used (30 and 50 °C), each with 3 ΔT values of 20, 30 and 40 °C.

Photoelectron Spectroscopy: The photoelectron spectroscopy measurements were performed in a custom designed multichamber UHV system at a base pressure of p ∼ 10⁻⁹ mbar, using a Phoibos 100 hemispherical analyzer (Specs). The UPS was done by using a monochromatic He source (VUV 5000, VG Scienta, hν = 21.22 eV) at an electron pass energy of 2 eV. A sample bias of −8 V was applied during measurements to observe the high energy cutoff. The experimental resolution at this low pass energy setting was only determined by thermal broadening and was in the range of 100 meV (ΔE = 4 k_BT).

Measurements of the unoccupied DOS were performed by inverse photoelectron spectroscopy. Here, a low energy electron gun (ELG-2, Kimball) was used at 2 μA emission current together with a bandpass photon detector (SrF_2/NaCl bandpass, IPES 2000, Omnivac). The energy resolution, as determined from the width of an Ag Fermi edge, was ≈ 600 meV. For all the measurements, the samples were transferred into the ultrahigh vacuum system under nitrogen atmosphere and were therefore not exposed to air.

X-Ray Photoelectron Spectroscopy: XPS measurements were carried out with a PHI 5000 VersaProbe III system fitted with an Al Ka excitation source (hν = 1486.6 eV) and a dual neutralizer (electron gun and Ar⁺) at 10⁻¹⁰ mbar. An X-ray source diameter of 100 mm was used to locally excite the samples; the corresponding photoemission with 45° take-off angle was collected at a multichannel analyzer. The survey and detailed spectra were measured with pass energies of 224 and 26/55 eV, respectively. The standard deviation on the reported energy values was ±0.1 eV. The spectra were analyzed with a Multipak software pack provided by the manufacturers. All emission signals were referenced to adventitious C 1s peak at 284.8 eV or the Au 4f7/2 peak at 84.0 eV. The samples were transported to the instrument using a N_2-filled transport vessel to avoid air/O_2 contamination. For quantitative analysis, the background of all spectra was corrected using the Shirley function.

Organic Field-Effect Transistor Measurements: Bottom gate/bottom contact organic field effect transistors (OFET Gen4) were purchased from Fraunhofer IPMS. N-doped silicon (doping at the surface n ∼ 3×10^{17} cm⁻³) was used as the surface and gate electrode. The dielectric consists of a 230 ± 10 nm layer of silicon oxide. Each substrate consisted of 16 devices with a constant channel width W of 10 mm and varying channel lengths L of 2.5 − 20 μm. The source and drain electrodes were a 30 nm thick gold layer on a 10 nm ITO adhesion layer. The devices were prepared by cleaning in acetone and subsequently in isopropanol in an ultrasonic bath for 15 min, followed by 15 min treatment in an ozone oven at 50 °C. The SiO_2 surface was passivated by 2 h treatment in hexamethylenedisilazane vapor at 100 °C. The devices were rinsed with isopropanol and dried with nitrogen. Thin polymer films were spun cast from 5 mg mL⁻¹ HFIP solutions at a spinning speed of 3000 rpm under ambient conditions. All devices were stored and measured under nitrogen atmosphere. The I–V characteristics were measured using an Agilent B1500 semiconductor parameter analyzer. Using Equation 1 the charge carrier mobility μ was calculated from the slope of the $(I_D)^{0.5}$–V_G plots, where V_t was the threshold voltage and C_i the SiO_2 insulator capacitance.

$$I_D = \frac{W}{2L} C_i \mu (V_G - V_t)^2 \tag{1}$$

Grazing-Incidence Small-Angle X-Ray Scattering: Grazing-incidence small-angle x-ray scattering (GIWAXS) on neat films coated of silicon substrates was performed in vacuum at RT on a laboratory system at the University of Bayreuth (Xeuss 3.0, Xenocs SAS, Grenoble, France) with a Cu Kα source (λ = 1.54 Å), a Dectris EIGER 2R 1 m detector, and a sample-to-detector distance of 52.5 mm. Scattering experiments were carried out on 0.5 cm by 0.5 cm Si/SiOₓ substrates due to decreased scattering background compared to glass. Q-profiles are cake cuts covering an azimuthal angle of 70°–110° for the cuts in the vertical direction and 0°–20° as well as 160°–180° for the cuts in the horizontal direction.

Matrix-Assisted Laser Desorption/Ionization Time-Of-Flight Mass Spectroscopy (MALDI-ToF MS): MALDI-ToF measurements were performed using a Bruker AutoFlex Max mass spectrometer equipped with a Smartbeam II laser. The analyte was embedded in the matrix material trans-2-[3-(4-tert-Butylphenyl)-2-methyl-2-propenylidene] malononitrile (DCTB) or dithranol in the matrix:analyte mass ratio 10:1.

Atomic Force Microscopy: The polymer films were characterized by tapping mode atomic force microscopy (AFM) in air/under ambient

**ADVANCED
SCIENCE NEWS**

www.advancedsciencenews.com

**ADVANCED
FUNCTIONAL
MATERIALS**

www.afm-journal.de

conditions using a Dimension Icon (Bruker Nano Inc.) equipped with a NanoScope V controller. AFM cantilevers (OMCL-AC160-TS-R3) with a nominal spring constant of 26 N m^{-1} and a typical resonant frequency of 300 kHz, were purchased from Olympus. Tapping Mode AFM images were acquired at scan sizes of 2 µm using a scan rate of 1 Hz and a pixel density of 512 pixels. The AFM height sensor and phase images were processed with NanoScope Analysis 1.80 (Bruker Nano Inc.).

Chemicals: Solvents were purchased from abcr, Germany and used as received. Deuterated DSMO (99.8 %) and D$_2$O (99.95 %) was supplied by Deutero, Germany. Lithium carbonate (≥99 %), potassium carbonate (≥99 %), rubidium carbonate (99.8 %) and cesium carbonate (≥99 %) were purchased from Sigma–Aldrich, USA, sodium carbonate (99.5 %) was purchased from Grüssing, Germany. The carbonates were dried at 200 °C under a high vacuum and stored under inert atmosphere until further use. CsHCO$_3$ (99.99 %) was purchased from Alfa Aesar, USA. N-DMBI (98 %) was sourced from Sigma–Aldrich. Tetraethylammonium carbonate was synthesized by bubbling CO$_2$ through a 25 wt.% tetraethylammonium hydroxide solution in methanol at rt for 12 h. The solvent was removed under vacuum, the educt was dried under vacuum at 75 °C for 3 d and stored under N$_2$ until further use. ^{1}H-NMR (300 MHz, DMSO-d_6, δ, referenced to residual solvent peak at 2.54 ppm): 3.21 (m, 8H, -CH$_2$-), 1.15 (m, 11H, -CH$_3$); ^{13}C-NMR (300 MHz, DMSO-d_6, δ, referenced to residual solvent peak at 39.53 ppm): 51.4 (-CH$_2$-), 7.13 (-CH$_3$); (Figures S19 and S20, Supporting Information). Monomer and polymer synthesis are given in the Supporting Information. The various steps of sidechain synthesis, polymerization etc. were adapted from reports of Thelakkat et al., Reynolds et al., and LeClerc et al. and the procedure was optimized for microwave synthesis, followed by Soxhlet extraction for oligomer, catalyst, and additive removal.[79–81] The polymer was then again precipitated in water and methanol to ensure quantitative removal of Cs$_2$CO$_3$ residues, as proven via XPS (Figure S21, Supporting Information). The molecular mass of the resulting polymer was determined to be 20.6 kg mol^{-1} with a dispersity of 1.8 via GPC (HFIP, PMMA standards, Figure S22, Supporting Information).

Supporting Information

Supporting Information is available from the Wiley Online Library or from the author.

Acknowledgements

Conflict of Interest

The authors declare no conflict of interest.

Data Availability Statement

The data that support the findings of this study are available in the supplementary material of this article.

[1] X. Xu, L. Yu, H. Meng, L. Dai, H. Yan, R. Li, Q. Peng, *Adv. Funct. Mater.* **2022**, *32*, 2108797.

[2] P. H. Wöbkenberg, D. D. C. Bradley, D. Kronholm, J. C. Hummelen, D. M. de Leeuw, M. Cölle, T. D. Anthopoulos, *Synth. Met.* **2008**, *158*, 468.

[3] F. Rodella, R. Saxena, S. Bagnich, D. Banevičius, G. Kreiza, S. Athanasopoulos, S. Juršėnas, *J. Mater. Chem. C* **2021**, *12*, 17471.

[4] M. Goel, M. Siegert, G. Krauss, J. Mohanraj, A. Hochgesang, D. C. Heinrich, M. Fried, J. Pflaum, M. Thelakkat, *Adv. Mater.* **2020**, *32*, 2003596.

[5] H. Un, S. A. Gregory, S. K. Mohapatra, M. Xiong, E. Longhi, Y. Lu, S. Rigin, S. Jhulki, C. Yang, T. V. Timofeeva, J. Wang, S. K. Yee, S. Barlow, S. R. Marder, J. Pei, *Adv. Energy Mater.* **2019**, *9*, 1900817.

[6] J. Mohanraj, M. Stihl, E. Simon, O. von Sicard, G. Schmidt, M. Fleischer, C. Neuber, M. Thelakkat, *ACS Appl. Energy Mater.* **2019**, *2*, 3469.

[7] M. Goel, C. D. Heinrich, G. Krauss, M. Thelakkat, *Macromol. Rapid Commun.* **2019**, *40*, 1800915.

[8] C. B. Nielsen, M. Turbiez, I. McCulloch, *Adv. Mater.* **2013**, *25*, 1859.

[9] X. Guo, M. D. Watson, *Org. Lett.* **2008**, *10*, 5333.

[10] H. Sun, X. Guo, A. Facchetti, *Chem* **2020**, *6*, 1310.

[11] Z. Yuan, B. Fu, S. Thomas, S. Zhang, G. DeLuca, R. Chang, L. Lopez, C. Fares, G. Zhang, J.-L. Bredas, E. Reichmanis, *Chem. Mater.* **2016**, *28*, 6045.

[12] C. J. Mueller, C. R. Singh, M. Fried, S. Huettner, M. Thelakkat, *Adv. Funct. Mater.* **2015**, *25*, 2725.

[13] D. Qu, T. Qi, H. Huang, *J. Energy Chem.* **2021**, *59*, 364.

[14] H. Yan, Z. Chen, Y. Zheng, C. Newman, J. R. Quinn, F. Dötz, M. Kastler, A. Facchetti, *Nature* **2009**, *457*, 679.

[15] T. Kono, D. Kumaki, J. Nishida, S. Tokito, Y. Yamashita, *Chem. Commun.* **2010**, *46*, 3265.

[16] T. Lei, J.-Y. Wang, J. Pei, *Acc. Chem. Res.* **2014**, *47*, 1117.

[17] L. Bürgi, M. Turbiez, R. Pfeiffer, F. Bienewald, H.-J. Kirner, C. Winnewisser, *Adv. Mater.* **2008**, *20*, 2217.

[18] M. M. Durban, P. D. Kazarinoff, C. K. Luscombe, *Macromolecules* **2010**, *43*, 6348.

[19] W. Khelifi, H. Awada, S. Blanc, G. H. Roche, L. Hirsch, B. Oboho, F. Castet, A. Bousquet, C. Lartigau-Dagron, *Appl. Sci.* **2022**, *12*, 4494.

[20] U. Salzner, *J. Chem. Phys.* **2021**, *154*, 054309.

[21] T. Hasegawa, M. Ashizawa, J. Hiyoshi, S. Kawauchi, J. Mei, Z. Bao, H. Matsumoto, *Polym. Chem.* **2016**, *7*, 1181.

[22] Y. Wang, T. Hasegawa, H. Matsumoto, T. Michinobu, *J. Am. Chem. Soc.* **2019**, *141*, 3566.

[23] Y. Shi, H. Guo, M. Qin, Y. Wang, J. Zhao, H. Sun, H. Wang, Y. Wang, X. Zhou, A. Facchetti, X. Lu, M. Zhou, X. Guo, *Chem. Mater.* **2018**, *30*, 7988.

[24] S. Griggs, A. Marks, H. Bristow, I. McCulloch, *J. Mater. Chem. C* **2021**, *9*, 8099.

[25] K. H. Hendriks, G. H. L. Heintges, M. M. Wienk, R. A. J. Janssen, *J. Mater. Chem. A* **2014**, *2*, 17899.

[26] S.-W. Chang, T. Muto, T. Kondo, M.-J. Liao, M. Horie, *Polym J* **2017**, *49*, 113.

[27] G. Krauss, A. Hochgesang, J. Mohanraj, M. Thelakkat, *Macromol. Rapid Commun.* **2021**, *42*, 2100443.

**ADVANCED
SCIENCE NEWS**

www.advancedsciencenews.com

**ADVANCED
FUNCTIONAL
MATERIALS**

www.afm-journal.de

[28] D. Kiefer, A. Giovannitti, H. Sun, T. Biskup, A. Hofmann, M. Koopmans, C. Cendra, S. Weber, L. J. Anton Koster, E. Olsson, J. Rivnay, S. Fabiano, I. McCulloch, C. Müller, *ACS Energy Lett.* **2018**, *3*, 278.

[29] K. Walzer, B. Maennig, M. Pfeiffer, K. Leo, *Chem. Rev.* **2007**, *107*, 1233.

[30] Z. Bin, J. Li, L. Wang, L. Duan, *Energy Environ. Sci.* **2016**, *9*, 3424.

[31] Y. Sun, C. Di, W. Xu, D. Zhu, *Adv. Electron. Mater.* **2019**, *5*, 1800825.

[32] O. Bardagot, C. Aumaître, A. Monmagnon, J. Pécaut, P.-A. Bayle, R. Demadrille, *Appl. Phys. Lett.* **2021**, *118*, 203904.

[33] P. Wei, J. H. Oh, G. Dong, Z. Bao, *J. Am. Chem. Soc.* **2010**, *132*, 8852.

[34] Y. Zeng, W. Zheng, Y. Guo, G. Han, Y. Yi, *J. Mater. Chem. A* **2020**, *8*, 8323.

[35] C.-I. Wu, C.-T. Lin, Y.-H. Chen, M.-H. Chen, Y.-J. Lu, C.-C. Wu, *Appl. Phys. Lett.* **2006**, *88*, 152104.

[36] K. C. Kwon, K. S. Choi, B. J. Kim, J.-L. Lee, S. Y. Kim, *J. Phys. Chem. C* **2012**, *116*, 26586.

[37] M.-H. Chen, D.-S. Leem, C. T. Lin, G. R. Lee, T.-W. Pi, J.-J. Kim, C.-I. Wu, in (Eds.: F. So, C. Adachi), xx, San Diego, CA **2008**, 70511C.

[38] A. Barbot, C. Di Bin, B. Lucas, B. Ratier, M. Aldissi, *J. Mater. Sci.* **2013**, *48*, 2785.

[39] J. Huang, Z. Xu, Y. Yang, *Adv. Funct. Mater.* **2007**, *17*, 1966.

[40] J. S. Yang, D. C. Choo, T. W. Kim, Y. Y. Jin, J. H. Seo, Y. K. Kim, *Thin Solid Films* **2010**, *518*, 6149.

[41] H.-H. Liao, L.-M. Chen, Z. Xu, G. Li, Y. Yang, *Appl. Phys. Lett.* **2008**, *92*, 173303.

[42] P.-C. Kao, J.-H. Lin, J.-Y. Wang, C.-H. Yang, S.-H. Chen, *Synth. Met.* **2010**, *160*, 1749.

[43] J. S. Swensen, *J. Photon. Energy* **2011**, *1*, 011008.

[44] T.-W. Lee, T. Noh, B.-K. Choi, M.-S. Kim, D. W. Shin, J. Kido, *Appl. Phys. Lett.* **2008**, *92*, 043301.

[45] J.-W. Ma, S.-W. Hwang, C.-C. Chang, S. F. Hsu, C. H. Chen, *SID Symposium Digest* **2006**, *37*, 964.

[46] J. Liu, M. P. Garman, J. Dong, B. van der Zee, L. Qiu, G. Portale, J. C. Hummelen, L. J. A. Koster, *ACS Appl. Energy Mater.* **2019**, *2*, 6664.

[47] Z. Bin, G. Dong, P. Wei, Z. Liu, D. Zhang, R. Su, Y. Qiu, L. Duan, *Nat. Commun.* **2019**, *10*, 866.

[48] A. Erhardt, A. Hochgesang, Christopher R. McNeill, M. Thelakkat, *Adv. Electron. Mater.* **2023**, 2300026.

[49] K. N. Wood, G. Teeter, *ACS Appl. Energy Mater* **2018**, *1*, 4493.

[50] A. Shchukarev, D. Korolkov, *Open Chemistry* **2004**, *2*, 347.

[51] T. R. Gengenbach, G. H. Major, M. R. Linford, C. D. Easton, *J. Vac. Sci. Techno. A* **2021**, *39*, 013204.

[52] K. C. Kwon, K. S. Choi, B. J. Kim, J.-L. Lee, S. Y. Kim, *J. Phys. Chem. C* **2012**, *116*, 26586.

[53] G. M. Bancroft, H. W. Nesbitt, R. Ho, D. M. Shaw, J. S. Tse, M. C. Biesinger, *Phys. Rev. B* **2009**, *80*, 075405.

[54] M. C. Ruiz-Cañas, H. I. Quintero, L. M. Corredor, E. Manrique, A. R. Romero Bohórquez, *Polymers* **2020**, *12*, 1152.

[55] P. Wei, Z. Shen, X. Qin, P. Zhang, L. Bu, Q. Chen, S. V. Roth, G. Lu, *Small* **2022**, *18*, 2105896.

[56] J. A. Gardella, S. A. Ferguson, R. L. Chin, *Appl. Spectrosc.* **1986**, *40*, 224.

[57] W. R. Salaneck, H. R. Thomas, *Solid State Commun.* **1978**, *27*, 685.

[58] F.-C. Chen, J.-L. Wu, S. S. Yang, K.-H. Hsieh, W.-C. Chen, *J. Appl. Phys.* **2008**, *103*, 103721.

[59] W. Hage, A. Hallbrucker, E. Mayer, *J. Am. Chem. Soc.* **1993**, *115*, 8427.

[60] J.-H. Wang, C.-C. Cheng, O. Altukhov, F.-C. Chang, S.-W. Kuo, *Polymers* **2013**, *5*, 937.

[61] M. Rayung, M. M. Aung, M. S. Su'ait, L. Chuah Abdullah, A. Ahmad, H. N. Lim, *ACS Omega* **2020**, *5*, 14267.

[62] H.-D. Jin, F. Zheng, W.-L. Xu, W.-H. Yuan, M.-Q. Zhu, X.-T. Hao, *J. Phys. D: Appl. Phys.* **2014**, *47*, 505502.

[63] H. Shirakawa, S. Ikeda, *Polym J* **1971**, *2*, 231.

[64] R. D. Shannon, *Acta Cryst A* **1976**, *32*, 751.

[65] D. Liu, T. Thomas, H. Gong, F. Li, Q. Li, L. Song, T. Azhagan, H. Jiang, M. Yang, *Org. Biomol. Chem.* **2019**, *17*, 9367.

[66] C. Gaul, S. Hutsch, M. Schwarze, K. S. Schellhammer, F. Bussolotti, S. Kera, G. Cuniberti, K. Leo, F. Ortmann, *Nature Mater* **2018**, *17*, 439.

[67] I. Salzmann, G. Heimel, M. Oehzelt, S. Winkler, N. Koch, *Acc. Chem. Res.* **2016**, *49*, 370.

[68] H. Méndez, G. Heimel, S. Winkler, J. Frisch, A. Opitz, K. Sauer, B. Wegner, M. Oehzelt, C. Röthel, S. Duhm, D. Többens, N. Koch, I. Salzmann, *Nat. Commun.* **2015**, *6*, 8560.

[69] D. M. de Leeuw, M. M. J. Simenon, A. R. Brown, R. E. F. Einerhand, *Synth. Met.* **1997**, *87*, 53.

[70] G. Ye, J. Liu, X. Qiu, S. Stäter, L. Qiu, Y. Liu, X. Yang, R. Hildner, L. J. A. Koster, R. C. Chiechi, *Macromolecules* **2021**, *54*, 3886.

[71] Z. Peng, L. Ye, H. Ade, *Mater. Horiz.* **2022**, *9*, 577.

[72] G. Zuo, X. Liu, M. Fahlman, M. Kemerink, *Adv. Funct. Mater.* **2018**, *28*, 1703280.

[73] Y. Zou, D. Huang, Q. Meng, C. Di, D. Zhu, *Org. Electron.* **2018**, *56*, 125.

[74] S. Wang, H. Sun, T. Erdmann, G. Wang, D. Fazzi, U. Lappan, Y. Puttisong, Z. Chen, M. Berggren, X. Crispin, A. Kiriy, B. Voit, T. J. Marks, S. Fabiano, A. Facchetti, *Adv. Mater.* **2018**, *30*, 1801898.

[75] J. Liu, G. Ye, B. van der Zee, J. Dong, X. Qiu, Y. Liu, G. Portale, R. C. Chiechi, L. J. A. Koster, *Adv. Mater.* **2018**, *30*, 1804290.

[76] C.-Y. Yang, W.-L. Jin, J. Wang, Y.-F. Ding, S. Nong, K. Shi, Y. Lu, Y.-Z. Dai, F.-D. Zhuang, T. Lei, C.-A. Di, D. Zhu, J.-Y. Wang, J. Pei, *Adv. Mater.* **2018**, *30*, 1802850.

[77] X. Yan, M. Xiong, J.-T. Li, S. Zhang, Z. Ahmad, Y. Lu, Z.-Y. Wang, Z.-F. Yao, J.-Y. Wang, X. Gu, T. Lei, *J. Am. Chem. Soc.* **2019**, *141*, 20215.

[78] A. Tripathi, Y. Lee, S. Lee, H. Y. Woo, *J. Mater. Chem. C* **2022**, *10*, 6114.

[79] G. Krauss, F. Meichsner, A. Hochgesang, J. Mohanraj, S. Salehi, P. Schmode, M. Thelakkat, *Adv. Funct. Mater.* **2021**, *31*, 2010048.

[80] R. M. W. Wolfe, J. R. Reynolds, *Org. Lett.* **2017**, *19*, 996.

[81] J.-R. Pouliot, L. G. Mercier, S. Caron, M. Leclerc, *Macromol. Chem. Phys.* **2013**, *214*, 453.